

# Loss-Resilient Thermal Image Fragmentation for LoRa Mesh IoT Networks

Krzysztof Sawicki, Tomasz Sosnowski, Mariusz Mścichowski

Military University of Technology, Institute of Optoelectronics, gen. S. Kaliskiego 2, 00-908 Warsaw, Poland

**Abstract:** Environmental monitoring using thermal cameras faces significant challenges in remote areas lacking cellular or fixed telecommunication infrastructure. This paper presents a novel fragmentation algorithm for transmitting low-resolution thermal images ( $32 \times 24$  pixels) through LoRa mesh networks characterized by limited throughput and high packet loss rates. The proposed three-tier fragmentation strategy divides thermograms into 16, 24, or 32 fragments with adaptive redundancy and loss compensation mechanisms. The algorithm implements pixel permutation to prevent clustered losses and hierarchical reconstruction using redundant information in the form of average values for different-sized regions. Simulation studies on 24 thermograms demonstrated gradual, linear quality degradation with increasing fragment losses. At near complete losses, the algorithm achieved RMSE temperature error of approximately  $2.3^{\circ}\text{C}$  (2.5 % relative error), PSNR drop from 53 dB to 30 dB, and maintained SSIM value at 0.3. The critical DIST metric, determining positional error of thermogram center of gravity, increased only to 0.25 pixels (less than 1 % of image size). Real-world verification in Warsaw's Meshtastic network with 200 devices confirmed practical utility. After transmitting 225 thermograms, receivers with 40 % fragment delivery still enabled reconstruction with average SSIM  $>0.6$  and DIST error  $<0.1$  pixels, demonstrating algorithm effectiveness for IoT monitoring applications.

**Keywords:** thermal imaging, image fragmentation, LoRa mesh networks, packet loss resilience, IoT monitoring

## 1. Introduction

Contemporary environmental, industrial, and security monitoring systems increasingly rely on temperature distribution analysis of observed scenes. Thermal cameras with  $32 \times 24$  pixel resolution, such as the MLX90640 (Fig. 1), have wide applications. They enable forest fire detection [1, 2], power infrastructure condition monitoring [3], and intruder identification in perimeter protection systems [4].

These systems are often deployed in challenging, hard-to-reach locations that lack both telecommunications and power infrastructure, such as large outdoor events, temporary military installations, mobile convoy operations, field command centers, and remote border surveillance points. In such scenarios, monitoring systems must be designed as “disposable” or semi-permanent installations that can operate autonomously without regular maintenance access. This operational requirement drives

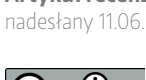
the need for cost-effective, energy-efficient solutions that can function reliably in resource-constrained environments.

However, a key challenge remains the transmission of thermograms from these remote areas lacking access to cellular networks or fixed telecommunications infrastructure. The combination of limited power budgets, harsh environmental conditions, and the absence of traditional communication channels necessitates innovative approaches to thermal data transmission that can maintain operational effectiveness while minimizing system complexity and cost.

Typical communication protocols, such as Wi-Fi or Bluetooth, are characterized by limited range and high energy consumption, which prevents their application in extensive IoT networks. An alternative is provided by LPWAN (Low-Power Wide-Area



**Fig. 1. The MLX90640 thermal camera**  
Rys. 1. Kamera MLX90640



Zezwala się na korzystanie z artykułu na warunkach licencji Creative Commons Uznanie autorstwa 4.0 Int.

Network) technologies, particularly LoRaWAN and Meshtastic, which combine long range (up to 15 km in open terrain) with low energy consumption. Unfortunately, the maximum theoretical throughput of these networks is only 37.5 kb/s [22], and the duty cycle limitations (< 10 %) applicable in the 868 MHz band (in Europe) further reduce the available channel capacity [23].

The problem of limited offered throughput is particularly severe in the case of thermal camera data transmission. A single thermogram with  $32 \times 24$  pixel resolution, encoded in 16-bit format, requires transmission of 1.5 kB of data. This exceeds both LoRa frame length limits (256 bytes) and practical mesh network capabilities under packet loss conditions reaching 30–50 %. The lack of corrective mechanisms leads to the loss of crucial information, such as heat source localization or temperature gradients essential in industrial applications.

The proposed solution utilizes a three-layer fragmentation algorithm adapted to LoRa network characteristics. Unlike classical data division methods, our approach considers:

- Adaptive redundancy – dynamic adjustment of fragment count (16, 24, or 32) depending on estimated or measured message delivery success rate.
- Information-rich area redundancy – multiple transmission of data from areas with large temperature gradients, crucial for anomaly detection, to increase probability of their successful delivery.
- Loss clustering avoidance – deliberate data mixing so that neighboring pixels are not transmitted in the same fragment.
- Loss compensation mechanism – reconstruction of missing fragments through interpolation based on neighboring pixels.

The algorithm's effectiveness was verified using four metrics: RMSE [5], PSNR, SSIM [6, 7], and the distance between thermogram centroids. The developed technology opens new possibilities in remote industrial monitoring, such as detecting overheating wind turbine components.

## 2. Problem analysis

Remote thermal monitoring does not pose a problem for modern telecommunications networks such as wired Gigabit Ethernet networks or wireless Wi-Fi or 5G networks. However, for such monitoring to be possible, extensive and expensive infrastructure is necessary. Thermal monitoring of areas where appropriate infrastructure is not available, for example monitoring of areas of military operations, poses a technological challenge. One of the solutions that comes to the rescue is LoRa technology [8].

### 2.1. LoRa technology

LoRa is a radio data transmission technology for long distances with low energy requirements. This also results in low throughput, which is why it is classified in the Low Power Wide Area Network (LPWAN) category. LoRa technology uses Chirp Spread Spectrum (CSS) modulation technique, which encodes information in the form of a signal with linearly increasing (or decreasing) frequency [9]. One symbol in CSS carries 5–13 bits of information and can last, depending on the parameters used, from several tens microseconds to several tens milliseconds. For this reason, LoRa offers low throughput from hundreds of bits per second to several tens kilobits per second.

A limitation of LoRa technology is also the maximum size of data that can be transmitted in one frame. It has been set at 256 bytes, which must also include application layer protocol headers. However, it should be remembered that frames

containing such large amounts of data are transmitted for a long time. Long transmission time means higher energy consumption by the device and increases the probability of radio collisions with transmission from another device. In practice, smaller data fragments are sent in one frame. Moreover, long frames are exposed to greater collision risk [10, 24].

LoRa operates in ISM bands. In Europe, these are the 433 MHz, 868 MHz, and 2.4 GHz bands [25]. The most popular of these bands, in the context of LoRa networks, is the 868 MHz band, in which, however, transmission time limitations apply. For the 869.40–869.65 MHz sub-band, transmission time is limited to 10 %, and the maximum transmitter power is limited to 500 mW (27 dBm) ERP (Effective Radiated Power). In the remaining sub-bands of the 868 MHz range, time and power limitations are much more restrictive [26]. Regulatory transmission time limitations reduce the actual channel capacity available to a single device. This means that devices using this band can transmit less data.

Radio networks with non-deterministic medium access encounter fundamental problems. This particularly applies to LoRa networks using CSMA/CA protocols. These problems significantly affect performance and reliability. The main problem is the inability to simultaneously transmit and receive on the same channel by a transmitter. Even if this were technically possible through additional equipment, the strength of the own transmission signal would be too great to detect a collision. Moreover, wireless channel conditions differ at the transmitter and receiver locations, which means that a collision detected by the transmitter may not indicate an actual collision at the receiver location [11].

Another important issue is the hidden terminal problem. It occurs when two stations located beyond the range of mutual detection attempt to simultaneously transmit data to a third station that is within range of both transmitters. Since neither of the two stations can detect the other's transmission, a collision occurs at the receiver location, leading to packet loss and reduced network performance [11, 12].

A problem of opposite nature to the hidden terminal is the exposed terminal problem, which occurs when a device refrains from transmitting data even though it could do so without interfering with another transmission. This situation occurs when a device receives a signal from a distant transmitter and incorrectly assumes it is too close to the target device to be able to transmit data. This problem leads to inefficient utilization of available communication channel bandwidth [13].

### 2.2. LoRa-based mesh networks

LoRa technology, particularly due to its low energy requirements and achieved ranges, has become a popular foundation for mesh networks. Currently, two competing LoRa-based mesh network solutions operate in Europe:

- Meshtastic — an open source project enabling the creation of decentralized mesh networks using the LoRa protocol, operating without the need for telecommunications infrastructure. The system uses a managed flood routing frame forwarding algorithm. Meshtastic supports encrypted communication and can accommodate hundreds of devices within a single network [27].
- MeshCore — a project competing with Meshtastic for decentralized networks, focusing on efficient multi-hop routing. MeshCore uses persistent routing paths that remain active until network topology changes, which significantly increases message delivery reliability. MeshCore is a much younger project than Meshtastic, poorly documented and with much lower popularity [28].

Mesh networks can compensate for some imperfections of LoRa technology:



- In the case of a well-chosen routing protocol and appropriately dense network, potential frame collisions are compensated by frame repetition through other network nodes.
- The allowable maximum transmit power of devices limits the ranges of possible transmissions, especially in terrain with obstacles (e.g., forest or buildings). The mesh network feature of forwarding received frames further allows increasing the effective range of transmitted data.

### 2.3. Analysis of thermograms as data intended for transmission

Thermograms constitute a specific type of image data that is characterized by unique structure and properties resulting from their nature. A thermogram is an image in which each point (pixel) is assigned a value representing temperature. Temperature values are often stored as 16- or 32-bit numbers.

The size of thermograms constitutes a key challenge for transmission systems with limited bandwidth. A thermogram with  $32 \times 24$  px resolution, in which values are stored in 16 bits, represents 1536 bytes of data. Transmission of only one thermogram of this size per second requires network throughput of 12.3 kb/s. This is more than the throughput values offered by most of the LPWAN networks. Specific properties of thermograms affect their compression possibilities. Thermal imaging data is characterized by high spatial correlation – neighboring pixels often have similar temperature values, which theoretically favors compression [14, 15]. However, requirements for maintaining measurement accuracy limit the application of aggressive lossy compression methods.

## 3. Method for low-resolution thermal image transmission

Transmission of thermograms in low-throughput LPWAN networks requires proper data preparation to minimize the negative impact of network imperfections:

- 1) The size of a single thermogram is too large to be transmitted in one LoRa frame. A  $32 \times 24$  px thermogram with 16 bits per pixel exceeds six LoRa frames at the maximum allowed size (256 bytes). To solve this problem, two actions must be taken: data fragmentation and compression.
- 2) During transmission in LPWAN networks, data loss may occur. Transmitted information should include redundant datasets enabling thermogram reconstruction even if partial data is lost.

### 3.1. Assumptions for the method

To develop the method for low-resolution thermal image transmission, the following assumptions must be adopted:

- 1) The thermal camera used is MLX90640. Recorded thermograms have  $32 \times 24$  px resolution [29].
- 2) The camera's NETD (Noise Equivalent Temperature Difference) is 0.1 K [29].
- 3) Transmission via LoRa in a Meshtastic mesh network.
- 4) The network does not guarantee message delivery reliability, and packet loss may exceed 50 %.
- 5) The network does not guarantee connection symmetry, and a return channel (from receiver to transmitter/camera) is unavailable.
- 6) Previously transmitted frames are not retransmitted.
- 7) Transmission is limited to 10 % duty cycle.
- 8) Thermograms represent scenes with temperature ranges from  $-20^{\circ}\text{C}$  to  $+70^{\circ}\text{C}$ .

The assumption of compatibility with Meshtastic network was driven by the presence of an established mesh network infrastructure in the local area, enabling practical validation of the proposed method.

The thermogram fragment preparation process, designed to optimize data for transmission over the mesh network, is shown in Fig. 2.

### 3.2. Thermogram fragmentation algorithm

In the proposed algorithm, the thermogram can be divided into  $N_p = 16, 24$ , or 32 fragments. This selection is a deliberate engineering choice driven by the properties of the thermal sensor and the constraints of the LoRa mesh network. The sensor produces a  $32 \times 24$  thermogram, resulting in a total of 768 pixels. The chosen values for  $N_p$  are integer divisors of 768, which is a prerequisite for fulfilling a key design principle: ensuring that each fragment contains an identical number of pixels (48, 32, or 24 pixels, respectively).

This choice represents a critical trade-off between packet size and protocol overhead. On one hand, using a smaller number of fragments (e.g., 8) would create larger data packets (96 pix each). Such large packets would have a higher probability of corruption or loss during transmission over a lossy channel and could approach the maximum payload size of a single LoRa frame. On the other hand, a significantly larger number of fragment (e.g., 48) would result in very small payloads (16 pix each). This approach would be inefficient, as the protocol overhead (headers, routing information, checksums) for each packet would become disproportionately large compared to the actual thermal data, wasting valuable bandwidth. Therefore, the values of 16, 24, and 32 are selected as a balanced compromise, optimizing for packet resilience without incurring excessive overhead.

Since these fragments need to be transmitted independently through the radio network with high packet loss, the fragmentation strategy also adheres to the following principles:

- Each fragment must contain the same number of pixels to ensure no fragment carries disproportionately more informational content.
- Fragments should avoid containing neighboring pixels from the original thermogram to prevent the formation of large, contiguous missing areas (loss clustering) when some fragments go undelivered.

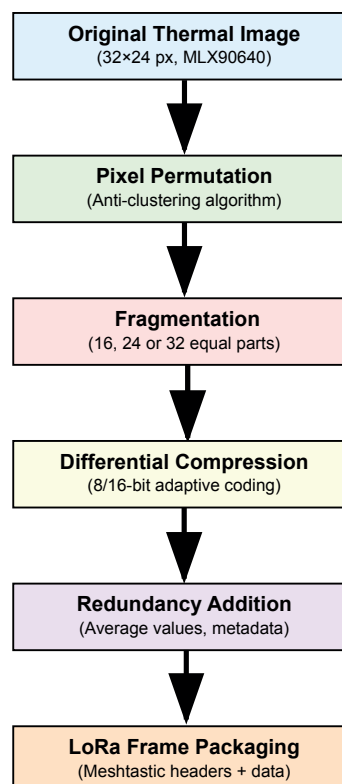


**Fig. 2. Thermal image fragmentation and compression pipeline for mesh networks**

Rys. 2. Proces fragmentacji i kompresji termogramów dla sieci mesh

The process of permuting the original thermogram  $\mathbf{T}_o$  relies on a pre-established, static 768-element permutation array, denoted as  $\mathbf{P}$ . Crucially, this array is not generated dynamically; it is determined a priori and must be identical for both the transmitting and receiving nodes to enable correct reconstruction. The array maps each original pixel position  $i$  from  $\mathbf{T}_o$  to a new position in the permuted thermogram  $\mathbf{T}_{\text{perm}}$ , such that  $\mathbf{T}_{\text{perm}}[\mathbf{P}[i]] = \mathbf{T}_o[i]$  for  $i \in 0, \dots, 767$ .

The construction of the static permutation array  $\mathbf{P}$  is performed using a structured sampling algorithm designed to distribute spatially adjacent pixels across the data stream. First, the  $32 \times 24$  thermogram space is conceptually partitioned into 16 non-overlapping rectangular regions, each measuring  $8 \times 6$  pixels. The algorithm then populates the array  $\mathbf{P}$  iteratively through a series of cycles.

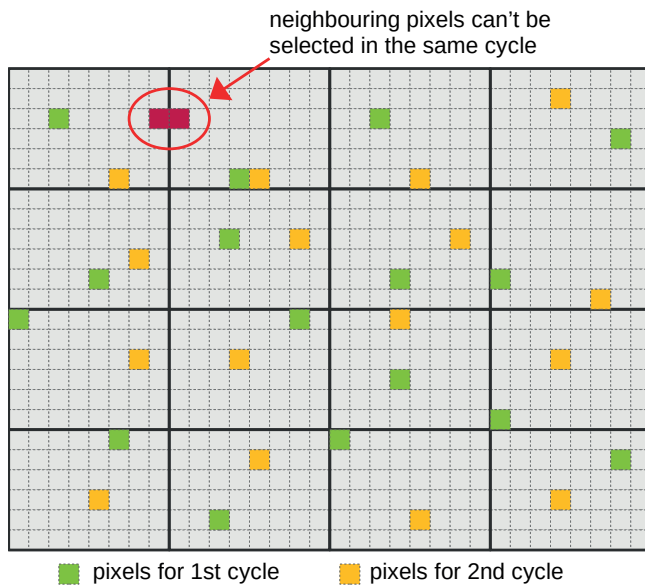


Fig. 3. Example of selecting pixels in cycles  
Rys. 3. Przykład wyboru pikseli w cyklach

In each cycle, the algorithm samples one pixel position from each of the 16 regions in a sequential manner. While the selection of a pixel position from within its designated region is random, the process is governed by a critical constraint: no two consecutive entries in the permutation array  $\mathbf{P}$  can correspond to pixels that are spatially adjacent in the original thermogram. This non-adjacency principle is illustrated in Fig. 3. The cyclic sampling continues until all 768 pixel positions have been exhausted and assigned a place in the array, thereby finalizing the deterministic permutation map  $\mathbf{P}$ .

This cyclic sampling continues until all pixel positions from every region have been included in the permutation array. The construction method ensures a fundamental property of the algorithm: regardless of the fragmentation strategy employed (16, 24, or 32 fragments), no individual fragment will contain spatially neighboring pixels that originate from the same rectangular region. This spatial distribution maximizes the reconstruction quality when fragments are lost during transmission.

This property is fundamental to the algorithm's resilience to fragment loss. Since a fragment does not contain adjacent pixels, its loss results in scattered, individual missing pixels rather than a contiguous block of missing data. This spatial distribution of lost data is crucial, as it allows for the effective reconstruction of each missing pixel's value through interpolation from its immediately surrounding, known neighbors.

Next, the array  $\mathbf{T}_{\text{perm}}$  is divided into  $N_p$  equal parts:  $[\mathbf{TP}_0, \dots, \mathbf{TP}_{N_p-1}]$ .

### 3.3. Thermogram compression

The thermal camera based on the MLX90640 module is supported by a library provided by the manufacturer [30]. This library returns an array of 768 values of type *float32* representing temperature given in °C. Analysis of the returned values indicates that the temperature resolution of the received thermograms is 0.1 °C, which is related to the camera's NETD parameter. Considering the assumption (section 3.1) of a limited temperature range, we obtain only 900 different values that pixels can take. Such a range of values can be stored using 16-bit numbers. In practice, however, the maximum dynamic range in the thermogram should not be expected. Observed scenes have a much smaller dynamic range, often not exceeding more than 25 °C. Assuming that we record temperature with a resolution of 0.1 °C, we have only 250 possible temperature values. These values can be stored using 8-bit numbers. The compression algorithm works as follows:

- 1) Input data preprocessing — Arrays of temperature values  $[\mathbf{TP}_0, \dots, \mathbf{TP}_{N_p-1}]$  expressed as single-precision floats are scaled by a factor of ten and converted to 16-bit integer arrays  $[\mathbf{T}_{\text{scaled} 0}, \dots, \mathbf{T}_{\text{scaled} N_p-1}]$ . This approach preserves temperature precision at 0.1 °C while maintaining computational efficiency for integer operations.
- 2) Arithmetic mean calculation — Compute the average value ( $T_{\text{avg}}$ ) of all samples in the original thermogram, serving as the reference value for differential representation. The calculated mean is also multiplied by 10 and quantized to a 16-bit integer format.
- 3) Differential transformation — Subtract the average value from each sample in the  $[\mathbf{T}_{\text{scaled} 0}, \dots, \mathbf{T}_{\text{scaled} N_p-1}]$  arrays. The resulting arrays  $[\mathbf{T}_{\text{diff16} 0}, \dots, \mathbf{T}_{\text{diff16} N_p-1}]$  contain differences relative to the mean which enables subsequent compression stages.
- 4) Adaptive bit-width encoding — For each differential value in  $\mathbf{T}_{\text{diff16}}$ , check if it fits within an 8-bit format. Values in the  $[-128, 127]$  range are directly copied to output arrays  $[\mathbf{T}_{\text{diff8} 0}, \dots, \mathbf{T}_{\text{diff8} N_p-1}]$ . Values exceeding this range are encoded as three-byte sequences: a zero-byte overflow indicator followed by the high and low bytes of the original 16-bit value. A special case is zero-value encoding, which requires a three-byte representation (0, 0, 0). While seemingly inefficient, this ensures decoding uniqueness while maintaining implementation simplicity.
- 5) Optimal representation selection — Compare sizes of  $\mathbf{T}_{\text{diff8}}$  and  $\mathbf{T}_{\text{diff16}}$  arrays. The algorithm selects the representation with smaller byte size, guaranteeing that compression never increases data size beyond the uncompressed differential representation.

### 3.4. Redundant information

The loss of any fragment during transmission prevents flawless thermogram reconstruction. However, adding a small amount of redundant data to each packet can compensate for potential losses. The redundant information includes:

- 1) The global average value of the entire thermogram.
- 2) Average values of the  $T_{\text{scaled}}$  thermogram computed over 12 rectangular  $8 \times 8$  px regions —  $AVG64 = [AVG64_0, \dots, AVG64_{11}]$ .
- 3) Average values of the  $T_{\text{scaled}}$  thermogram computed over 48 square  $4 \times 4$  px regions —  $AVG16 = [AVG16_0, \dots, AVG16_{47}]$ . Only  $N_r$  most significant values (e.g., 4) are selected from this array. Standard deviation values are calculated for the same squares, and averages from regions with the highest standard deviations are prioritized.

### 3.5. Data packetization

For data transmission, packets must be prepared in accordance with the LoRa protocol (maximum message size) and the selec-



ted Meshtastic network. The Meshtastic network requires the addition of an extra frame header, which contains the following information:

- 1) a 32-bit transmitter (source) station identifier,
- 2) a 32-bit receiver (destination) station identifier,
- 3) a 32-bit unique message identifier,
- 4) an octet containing information about the initial retransmission limit in the network (HopStart) and the current retransmission limit (HopLimit),
- 5) two additional octets reserved by the protocol.

To enable thermogram reconstruction, it has been established that each frame must contain not only the thermogram fragment data from the  $T_{\text{diff}_n}$  array but also the following metadata:

- 1) An 8-bit thermogram number enabling proper reassembly of received fragments.
- 2) An 8-bit fragment number  $N_f$  of the transmitted thermogram.
- 3) A 16-bit average value of the entire thermogram.
- 4) A 16-bit average value  $AVG64_n$  where  $n = (N_f + 8) \bmod N_p$ .
- 5) Two successive 16-bit average values from the  $N_f$  most significant  $AVG16$  entries.

Each frame must therefore contain 11 bytes of the Meshtastic network header, 8 bytes required for thermogram reconstruction, and the fragment data itself. The possible frame sizes are as follows:

- 1) when  $N_p = 16$ : from 67 to 115 bytes,
- 2) when  $N_p = 24$ : from 51 to 83 bytes,
- 3) when  $N_p = 32$ : from 43 to 67 bytes.

Frames prepared in this manner are transmitted to the Meshtastic network. Each frame is transmitted only once. The transmitter has no way of determining whether the frame has been received by any receiver.

The transmission time of a frame in a LoRa system is directly related to the data length and modulation parameters. The primary parameter affecting transmission time is the Spreading Factor (SF), which determines the number of bits transmitted in a single symbol [22, 8, 9]. The duration of a single symbol is given by the equation:

$$T_{\text{symb}} = \frac{2^{\text{SF}}}{\text{BW}} \quad (1)$$

where BW is the chirp signal bandwidth.

Data transmitted in LoRa is also subject to forward error correction (FEC) coding in 4/5, 4/6, 4/7, or 4/8 modes [16]. Additionally, a LoRa frame is preceded by an appropriate preamble and includes a LoRa header. To calculate the frame transmission time, it is necessary to determine the modulation parameters (SF, BW), coding rate, required preamble length  $\text{Preamble}_{\text{len}}$ , and the size of the data to be transmitted.

In the Meshtastic network, three sets of settings are most commonly used:

- 1) the default **LongFast**: SF = 11, BW = 250 kHz, CR = 4/5,  $\text{Preamble}_{\text{len}} = 16$ ,
- 2) **MediumFast**, used in large networks: SF = 9, BW = 250 kHz, CR = 4/5,  $\text{Preamble}_{\text{len}} = 16$ ,
- 3) **ShortFast**, which is used in very dense mesh networks (e.g. in Upper Silesia Region, Southern Poland): SF = 7, BW = 250 kHz, CR = 4/5,  $\text{Preamble}_{\text{len}} = 16$ .

Based on the data, the time required to transmit frames containing thermogram fragments can be determined, as described in [22]. The results are presented in Table 1.

By adhering to the 10 % transmission time limitation (duty cycle), we can calculate the maximum theoretical number of thermograms transmittable per hour:

$$N_{\text{mash}} = \left\lfloor \frac{3600s \cdot 0.1}{N_p \cdot t_{\text{tx min}}} \right\rfloor \quad (2)$$

where  $t_{\text{tx min}}$  is the transmission time of the shortest possible data frame for a given fragment count  $N_p$ . The results are summarized in Table 2.

**Tab. 1. Transmission time ranges (minimum–maximum) for frames in various LoRa modem operating modes [ms]**

Tab. 1. Czasy transmisji (min–max) ramek w różnych trybach pracy modemu LoRa [ms]

$N_p$	<b>LongFast</b>	<b>MediumFast</b>	<b>ShortFast</b>
16	624.640–985.088	184.832–291.328	56.960–92.288
24	501.760–739.328	147.968–219.648	45.696–69.248
32	444.160–624.640	137.728–184.832	39.552–56.960

**Tab. 2. Maximum theoretical hourly thermogram transmission capacity**

Tab. 2. Maksymalna teoretyczna liczba termogramów możliwa do przesłania w godzinę

$N_p$	<b>LongFast</b>	<b>MediumFast</b>	<b>ShortFast</b>
16	36	121	395
24	29	101	328
32	25	81	284

These values would represent network saturation. In networks with traffic from other stations, the thermogram transmission frequency must be reduced to avoid channel monopolization.

### 3.6. Data reconstruction

Data received by the receiver are usually incomplete. To reconstruct the thermogram, the following procedure is performed:

- 1) Decompression of data in packets – values stored as 8-bit are restored to 16-bit form. The average value of the original thermogram  $T_o$  is added to the obtained values. This is the inverse process of that described in section 3.3.
- 2) Generating the reconstructed thermogram matrix  $T_r$ , in which each pixel receives a value equal to the average of the original thermogram  $T_o$ . Since the average value is transmitted in each fragment, one received fragment is sufficient to initialize  $T_r$ .
- 3) Creating the status matrix  $C_r$  with dimensions identical to  $T_r$ , initially filled with zeros. The matrix stores information about the reconstruction method of each pixel: 1 – from a received fragment, 0 – requires interpolation.
- 4) Writing pixel values from received fragments to the appropriate positions in  $T_r$  based on the fragment number and permutation array. Positions filled from fragments are marked in  $C_r$  with the value 1.
- 5) Replacing missing pixels (marked as 0 in  $C_r$ ) with average values  $AVG64$  from corresponding  $8 \times 8$  px areas, if these values have been received.
- 6) Replacing remaining missing pixels with  $AVG16$  values from  $4 \times 4$  px areas, if available.
- 7) Interpolating missing pixels as a weighted average of available neighboring pixels in a  $3 \times 3$  neighborhood.

- 8) Correcting systematic errors by equalizing averages: calculating differences between  $AVG64_{rec}$ ,  $AVG16_{rec}$  and their corresponding original values, then correcting interpolated pixels by these differences.

The described reconstruction algorithm ensures hierarchical thermogram reconstruction, utilizing available information in order from least to most precise (Fig. 4). This multi-level approach — ranging from regional average values, through local interpolation, to local error correction—enables satisfactory reconstruction quality even with significant fragment loss. An example visualization of thermograms reconstructed from 1, 4, 8, 12, and 16 (out of 16) fragments is presented in Fig. 5.

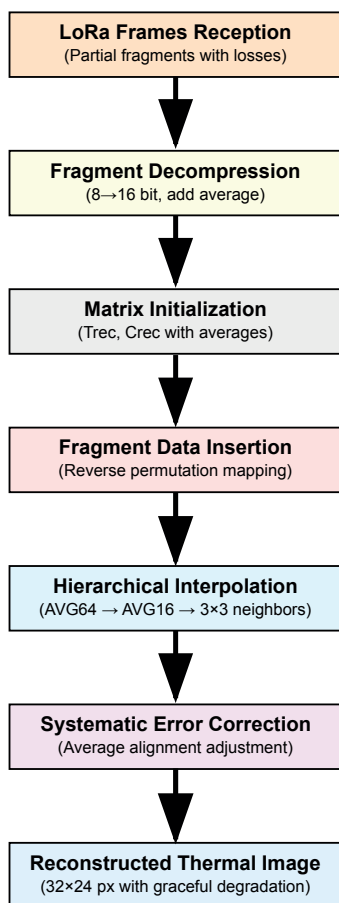


**Fig. 4.** The defragmentation and reconstruction process at the receiver side

Rys. 4. Proces defragmentacji i rekonstrukcji termogramu po stronie odbiornika w sieci mesh

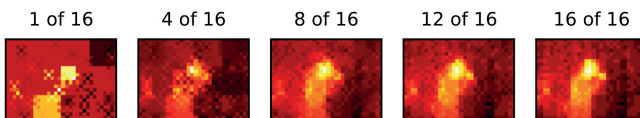


**Fig. 5.** A visualization of the proposed algorithm's. The quality of the reconstructed image improves as more fragments are received

Rys. 5. Wizualizacja działania algorytmu rekonstrukcji. Jakość obrazu rośnie wraz z liczbą pomyślnie odebranych fragmentów

## 4. Modeling algorithm operation

To evaluate the effectiveness of the algorithm, comprehensive experimental studies were conducted. A set of 24 different thermograms with a resolution of  $32 \times 24$  px recorded by the MLX90640 camera was used. The thermograms are shown in Fig. 6, and their parameters in Fig. 7. Each thermogram was subjected to the fragmentation process according to three variants of the algorithm (16, 24, and 32 fragments), followed by simulation of random fragment losses in radio transmission characteristic of LoRa mesh networks.

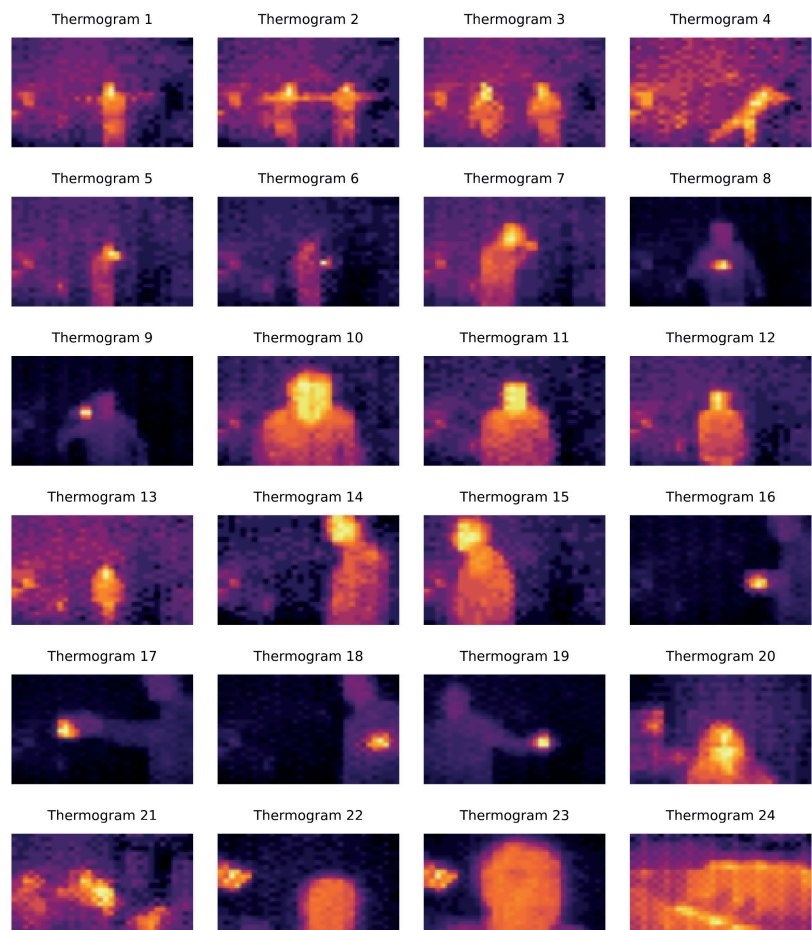


**Fig. 6.** A set of thermograms used in the experiment  
Rys. 6. Termogramy użyte w eksperymencie

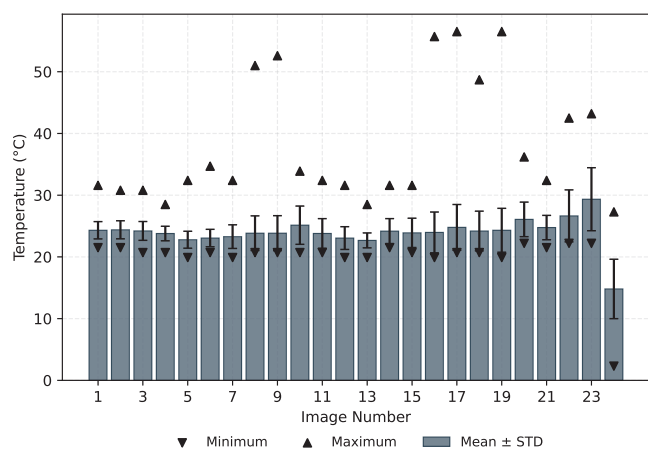


**Fig. 7.** Statistics of the thermogram's set  
Rys. 7. Statystyki użytych termogramów



The experiment involved systematic testing of various transmission loss levels, ranging from zero to the maximum values at which thermogram reconstruction remains possible. For each loss level, one thousand iterations of the experiment were performed to ensure the statistical reliability of the results. The random nature of fragment losses simulated actual radio propagation conditions in a mesh environment, where packet loss can arise from interference, signal attenuation, or collisions in the transmission medium.

The reconstruction quality was assessed using four key metrics: *RMSE*, *PSNR*, *SSIM*, and *DIST*. The Root Mean Square Error (*RMSE*) quantifies the average pixel-wise error between the original and reconstructed images [6, 7]:

$$RMSE = \sqrt{\frac{1}{MN} \sum_{i=1}^M \sum_{j=1}^N (T_o(i,j) - T_r(i,j))^2} \quad (3)$$

where:  $M$  and  $N$  — dimensions of the thermogram in pixels,  $T_o$  — original thermogram,  $T_r$  — reconstructed thermogram.

The Peak Signal-to-Noise Ratio (*PSNR*) measures the ratio of maximum signal power to reconstruction error, expressed in decibels [7, 17]:

$$PSNR = 10 \log_{10} \left( \frac{MAX^2}{MSE} \right) \quad (4)$$

where  $MAX$  is the maximum value a pixel can take in the thermogram. In the analyzed case,  $MAX = 70$ , which results from the maximum value of the assumed temperature range.

The Structural Similarity Index Measure (*SSIM*) evaluates perceptual similarity by comparing local patterns of pixel intensities [7, 17]:

$$SSIM(T_o, T_r) = \frac{(2\mu_{T_o}\mu_{T_r} + c_1)(2\sigma_{T_o T_r} + c_2)}{(\mu_{T_o}^2 + \mu_{T_r}^2 + c_1)(\sigma_{T_o}^2 + \sigma_{T_r}^2 + c_2)} \quad (5)$$

where:  $\mu_{T_o}$ ,  $\mu_{T_r}$  are the mean values of the thermograms,  $\sigma_{T_o}^2$ ,  $\sigma_{T_r}^2$  are the variances of the thermograms,  $\sigma_{T_o T_r}$  is the covariance between the thermograms,  $c_1 = (k_1 L)^2$ ,  $c_2 = (k_2 L)^2$  are stabilizing constants,  $L$  is the dynamic range of the pixels,  $k_1 = 0.01$ ,  $k_2 = 0.03$  [31].

The centroid distance (*DIST*) is the Euclidean distance between the centroids of the original ( $C_o$ ) and reconstructed ( $C_r$ ) thermograms:

$$RMSE = \sqrt{\frac{1}{MN} \sum_{i=1}^M \sum_{j=1}^N (T_o(i,j) - T_r(i,j))^2} \quad (6)$$

where  $C(T_o)_x$  and  $C(T_o)_y$  are the respective  $x$  and  $y$  coordinates of the original thermogram's centroid ( $C(T_o)$ ), and  $C(T_r)_x$  and  $C(T_r)_y$  are the coordinates for the reconstructed thermogram's centroid ( $C(T_r)$ ). A centroid coordinate is calculated as:

$$C(T) = \frac{\sum_{i=1}^M \sum_{j=1}^N j \cdot T(i,j)}{\sum_{i=1}^M \sum_{j=1}^N T(i,j)} \quad (7)$$

This metric is particularly relevant for thermal imaging applications where the center of mass often corresponds to the primary heat source or thermal anomaly of interest, making its preservation crucial for maintaining the semantic meaning of the thermal data. The displacement of the thermal centroid can significantly impact subsequent analysis tasks such as object detection, tracking, or temperature monitoring, especially in IoT scenarios where computational resources for complex post-processing are limited.

The results for all metrics are presented as a function of the transmission loss percentage, where each point on the plots represents the value averaged over multiple experimental repetitions for a given loss level (Figs. 8–11). This approach allows for an objective assessment of the algorithm's resilience to loss and the identification of the optimal fragmentation strategy depending on the transmission conditions.

The increase in temperature error to approximately 2.3 °C (Fig. 8), even under near-total loss conditions (reconstruction from 1 of 32 fragments), is relatively small. Considering the assumed temperature range of -20 °C to +70 °C, this represents a relative error of approximately 2.5 %.

The *PSNR* metric (Fig. 9) decreases from approx. 53 dB to approx. 30 dB at nearly 100 % fragment loss. This indicates acceptable reconstruction quality. *PSNR* values greater than

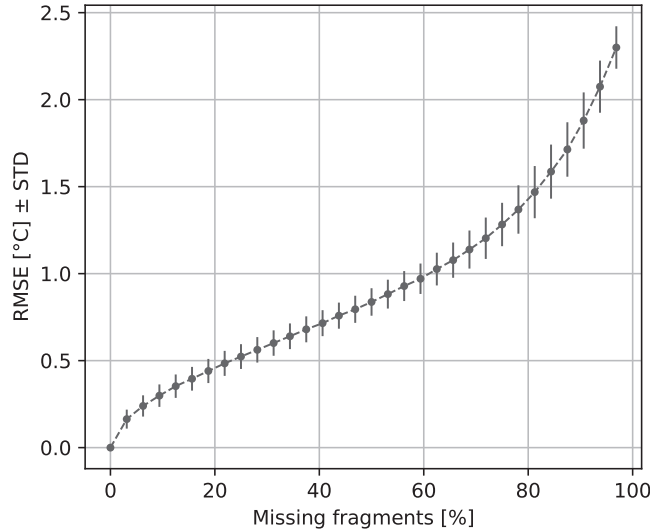


Fig. 8. *RMSE* value as a function of fragment loss  
Rys. 8. Wartość *RMSE* w funkcji strat fragmentów

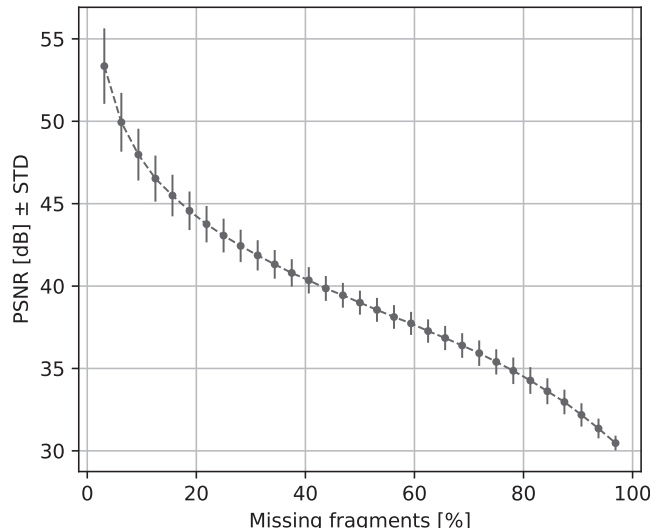


Fig. 9. *PSNR* value as a function of fragment loss  
Rys. 9. Wartość *PSNR* w funkcji strat fragmentów

30 dB are considered satisfactory in thermal imaging applications, which means the algorithm is useful even at 80–90 % loss [18].

The decrease in *SSIM* value (Fig. 10) from 1.0 to approx. 0.3 shows that the algorithm retains a significant portion of structural information, even at high loss rates. An *SSIM* value greater than 0.8 at 50 % loss suggests that key thermogram patterns are preserved [19].

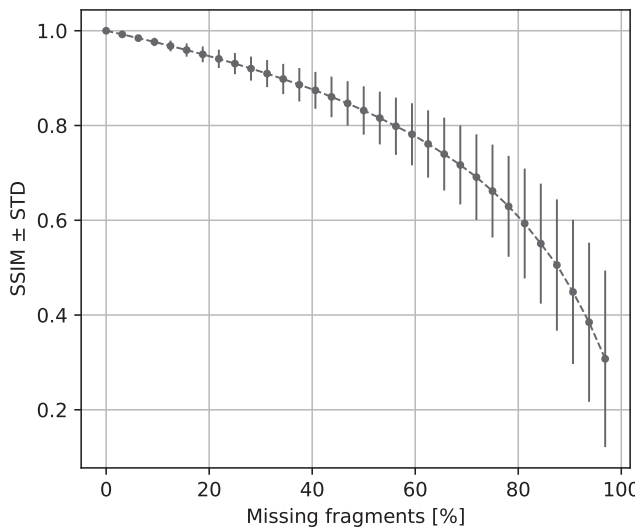


Fig. 10. SSIM value as a function of fragment loss  
Rys. 10. Wartość SSIM w funkcji strat fragmentów

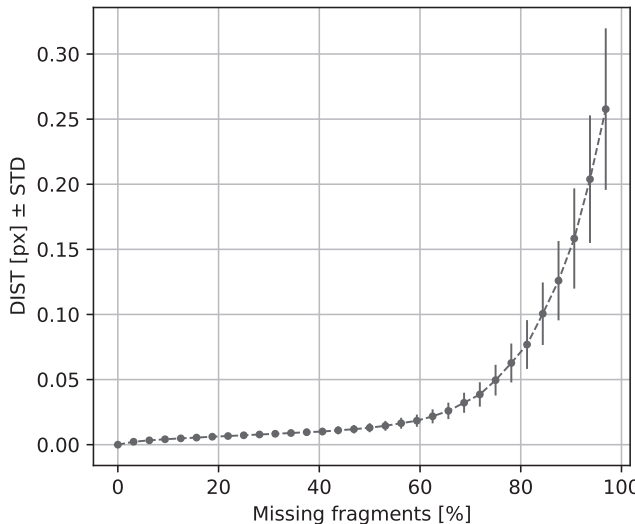


Fig. 11. DIST value as a function of fragment loss  
Rys. 11. Wartość DIST w funkcji strat fragmentów

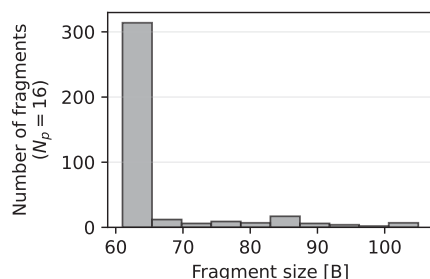


Fig. 12. Histogram of fragment sizes for  $N_p = 16$   
Rys. 12. Histogram rozmiarów fragmentów dla  $N_p = 16$

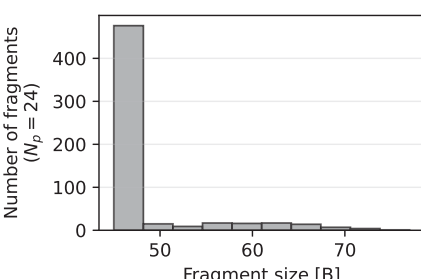


Fig. 13. Histogram of fragment sizes for  $N_p = 24$   
Rys. 13. Histogram rozmiarów fragmentów dla  $N_p = 24$

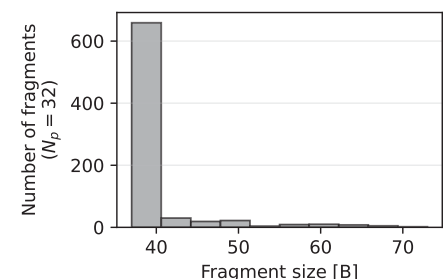


Fig. 14. Histogram of fragment sizes for  $N_p = 32$   
Rys. 14. Histogram rozmiarów fragmentów dla  $N_p = 32$

The key metric is *DIST* (Fig. 11). It increases to a value of approx. 0.25 px at near-total fragment loss. This measure is particularly important for object detection and their position within the thermogram. For a  $32 \times 24$  px thermogram, this represents a positional error of less than 1 % of the image size, which is a good result for localizing heat sources.

The metrics exhibit distinct degradation patterns as fragment loss increases. *RMSE* and *PSNR* demonstrate sharp degradation at very low loss rates followed by linear degradation, while *SSIM* and *DIST* maintain stable performance across low to moderate loss rates before experiencing accelerated deterioration only at high loss rates. This differential behavior is advantageous for the algorithm, as it ensures predictable performance across the operational range without sudden quality collapses under variable network conditions.

The algorithm's weakness only becomes apparent at loss rates exceeding 80 %, which in most network scenarios would signify a complete loss of connectivity.

## 5. Experiment using a real network

The thermogram fragmentation algorithm presented in the previous chapters was verified under real Meshtastic network conditions in an urban environment. The field experiment conducted in Warsaw had two objectives. The first was to investigate the practical effectiveness of the algorithm in real radio propagation conditions. The second was to assess the impact of fragmentation on the quality of thermogram reconstruction under packet loss. The Meshtastic network in Warsaw represents one of the larger urban networks in Europe. During the experiment, the network consisted of approximately 200 devices.

In the experiment, test thermograms were transmitted with division variants of  $N_p = 16$ , 24, and 32 fragments. Since the transmission was carried out using a live, community-driven Meshtastic network, the following operational assumptions were adopted to ensure minimal interference with its regular users:

- 1) adapting the LoRa modem operating mode to the parameters used in the network: SF = 9, BW = 250 kHz, CR = 4/5 (MediumFast mode),
- 2) scheduling transmissions exclusively during nighttime hours, from 21:00 to 6:00 local time,
- 3) setting long intervals between transmissions: 20 s between consecutive fragments and 240 s between consecutive thermograms,
- 4) configuring the maximum hop count for a transmitted frame to 7 (HopCount = 7).

The decision to limit transmissions to nighttime hours was a critical consideration. The network is a non-commercial project, built and maintained by volunteers in their personal time



and with their own financial resources. Its primary purpose is to serve the community's needs, which are concentrated during the daytime. By conducting the experiment during off-peak hours, we ensured that the additional load generated by our research would not disrupt regular network activity. The community was informed about the experiment beforehand, and not only were no objections raised, but several members also engaged actively in the process, underscoring the collaborative spirit of the project.

A total number of 225 thermograms were transmitted over five sessions (five nights). The set of transmitted thermograms was based on the 24 thermograms used in paragraph 4. The thermograms were sent sequentially, fragmented in three different ways. Seventy-five thermograms were sent fragmented into 16, 24, and 32 fragments, respectively. Each thermogram from the test group of 24 thermograms was sent at least 9 times.

A set of eight receiving stations was strategically positioned across the urban area to capture and log transmitted thermogram fragments.

The transmitted thermograms compressed well, and the fragment size was, in most cases, the smallest possible. Histograms of final fragment sizes in bytes (after fragmentation into  $N_p$  parts, compression and redundancy addition) are presented in Figs. 12, 13, and 14.

## 5.1. Hardware and software implementation

The transmitting device was an ESP32-S3 microcontroller with a Semtech SX1262 LoRa radio module. The MLX90640 camera was connected to the microcontroller. The device was powered by a single 1500 mAh Li-Ion battery. It was programmed in MicroPython as an autonomous unit. Transmission was carried

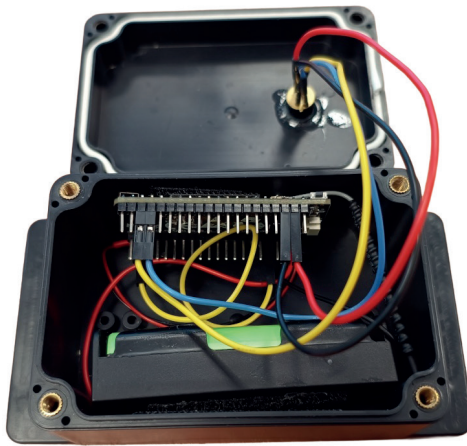


**Fig. 15. Equipment used for the experiment: Heltec Wireless Stick Lite development board with ESP32-S3 and SX1262, and MLX90640**  
Rys. 15. Sprzęt użyty do eksperymentu: płytka deweloperska Heltec Wireless Stick Lite z ESP32-S3 oraz SX1262 oraz kamera MLX90640



**Fig. 16. The assembled and closed in the box device with thermal camera**  
Rys. 16. Złożone i zamknięte urządzenie z kamerą termowizyjną

out during nighttime hours; at other times, the device was in deep sleep mode. The energy efficiency of the ESP32-S3 and SX1262 modules, combined with the deep sleep mode, allowed the entire experiment to be conducted without recharging the battery during its course. The completed device is shown in Figs. 15 and 16.

## 5.2. Results

Data receivers were labelled with letters A-H. In the charts, they are sorted according to their distance from the transmitting device, measured by the average number of hops that frames travel to reach the destination. Two receivers (A and B) received data directly from the transmitting device (Fig. 17).

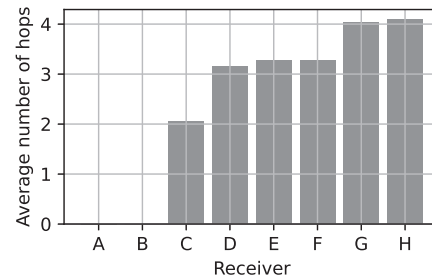


**Fig. 17. Average number of hops from the thermal camera transmitter to receivers**

Rys. 17. Średnia liczba skoków od nadajnika z kamerą termowizyjną do odbiorników

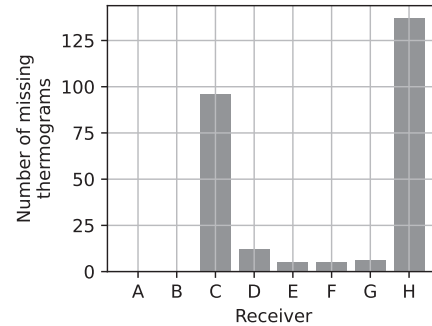


**Fig. 18. The number of missing thermograms on the receiver side**  
Rys. 18. Liczba nieodebranych termogramów

A characteristic of the used network is the lack of message delivery guarantee. This is noticeable in the chart of undelivered thermograms (Fig. 18). Receiver C, despite its relative proximity to the transmitter, did not receive 96 out of 225 thermograms. Meanwhile, the most distant receiver H did not receive 137 of them. The criterion for receiving a thermogram was the reception of at least one of its fragments. The lack of reception of entire thermograms could have resulted from variable network conditions – Meshtastic network nodes are operated by independent individuals and can be turned on and off at any unpredictable moments.

Thermograms were divided into 16, 24, or 32 fragments. This division also determines the size of the frames transmitted through the network. However, most fragments had the smallest size resulting from the fragmentation algorithm (Figs. 12, 13, and 14). Figure 19 shows the fragment delivery ratio for three values of  $N_p$ :

$$RCV_{ratio}(N_p) = \frac{R_{N_p}}{TN} \quad (8)$$

where  $R_{N_p}$  is the number of received fragments of thermograms divided into  $N_p$  parts, and  $TN$  is the number of thermograms for which at least one fragment was received.

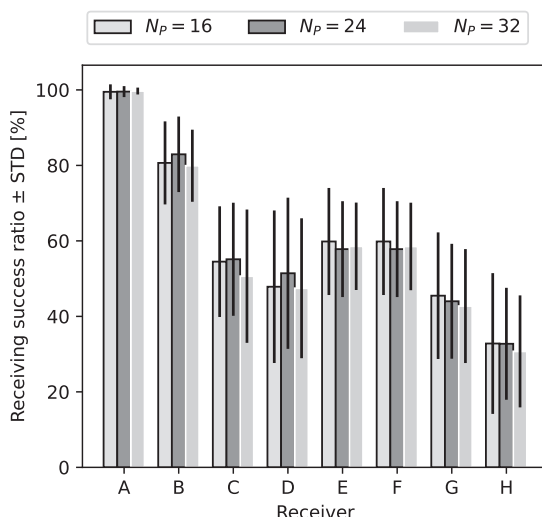


Fig. 19. Delivery ratio  $RCV_{ratio}$  to receivers  
Rys. 19. Współczynnik dostarczalności  $RCV_{ratio}$  do odbiorników

The results show no dependence of the delivery ratio  $RCV_{ratio}$  on fragment size, which is a significant finding of the experiment. Theoretically, one might expect larger fragments ( $N_p = 16$ ) to be more prone to loss than smaller ones ( $N_p = 32$ ), but empirical data do not confirm this. This suggests that under the tested network conditions, the main factor influencing losses is not the size of a single fragment but other network parameters. The fragment size constitutes only part of the frame size sent over the radio network. Since most fragments have the minimal possible size, their transmission times in MediumFast mode are as follows (for  $N_p = 16, 24, 32$  respectively): 184.832 ms, 147.968 ms, 137.728 ms. The frame for  $NP = 16$  is only 47.104 ms longer than the frame for  $NP = 32$ . Although the fragment size is twice as large, the transmission time increases by only 34 %.

The degradation of reception quality with distance is clearly visible – more distant receivers (with a higher number of hops) systematically show a lower fragment reception ratio. This confirms the expected behavior of mesh networks, where each additional hop introduces an increased risk of packet loss.

Figures 20–23 present the metric values  $RMSE$ ,  $PSNR$ ,  $SSIM$ , and  $DIST$  of thermograms received by individual receivers. Receivers A and B, which were placed relatively close to the transmitting device, received most of the transmitted thermograms in full, hence the average  $PSNR$  measure for them reached infinity. It is worth noting that data from receiver H, which on average received about 40 % of thermograms, still allowed reconstruction of thermograms with an average  $SSIM$  value greater than 0.6. The average  $DIST$  value, even with such high losses, remained within a range smaller than 0.1 pixel.

## 6. Summary

In recent years, there has been growing interest in the reliable transmission of image data over LoRa and mesh networks, with several approaches proposed to address the inherent limitations of low throughput and high packet loss. For instance [20] presented a scheme for reliable image transmission over LoRa networks, which combines image resizing, grid-based patching, and retransmission mechanisms to ensure data integrity. Their method relies on acknowledgements and retransmissions, which, while improving reliability, can significantly increase network traffic and energy consumption — an important consideration in battery-powered IoT deployments.

Other studies have explored the use of advanced compression schemes, such as WebP with Base64 encoding, to reduce the size of transmitted images and the total number of packets required [21]. However, these approaches typically target general-purpose images and do not exploit the specific statistical properties of thermal images, such as high spatial correlation and limited dynamic range, which can be leveraged for more efficient encoding and reconstruction.

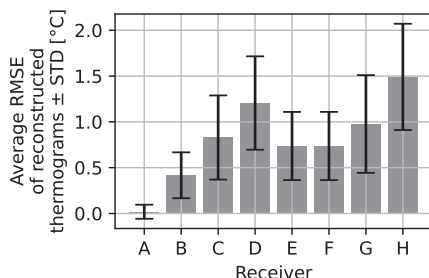


Fig. 20. Average  $RMSE$  values of received thermograms  
Rys. 20. Uśrednione wartości  $RMSE$  odebranych termogramów

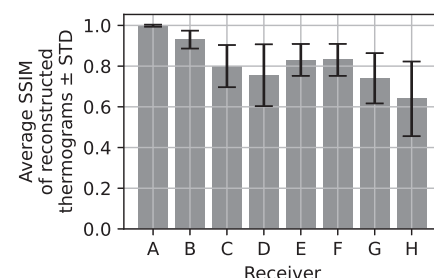


Fig. 22. Average  $SSIM$  values of received thermograms  
Rys. 22. Średnie wartości  $SSIM$  odebranych termogramów

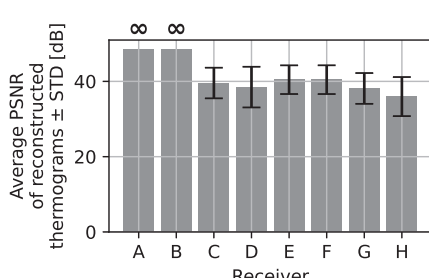


Fig. 21. Average  $PSNR$  values of received thermograms  
Rys. 21. Uśrednione wartości  $PSNR$  odebranych termogramów

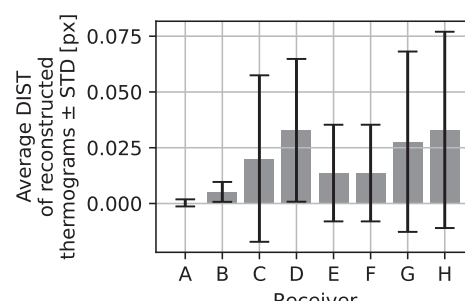


Fig. 23. Average  $DIST$  values of received thermograms  
Rys. 23. Średnie wartości  $DIST$  odebranych termogramów

**Tab. 3. Comparison of selected approaches for image transmission over LoRa networks**

Tab. 3. Porównanie wybranych rozwiązań do transmisji obrazów w sieciach LoRa

Feature	Single-hop method [20]	Multi-hop method [21]	This work
Retransmissions/Acknowledgements	Yes	Yes	No
Compression Scheme	Resizing, grid patch	WebP, Base64	Differential, adaptive
Mesh Topology Support	Limited	Limited	Full (Meshtastic)
Loss Clustering Avoidance	No	No	Yes
Hierarchical Reconstruction	No	No	Yes
Real-world Mesh Validation	No	No	Yes (Warsaw network)

In contrast to retransmission-based protocols, the algorithm proposed in this work adopts a loss-resilient, redundancy-driven strategy designed to the characteristics of thermal images and the constraints of LoRa mesh networks. By employing adaptive fragmentation, pixel permutation, and hierarchical reconstruction using regional averages, the method achieves gradual quality degradation with increasing fragment loss, without the need for acknowledgements or retransmissions. This is particularly advantageous in mesh topologies where reverse channels may be unavailable or unreliable.

Moreover, while [30] introduced a multi-hop LoRa mesh network with a revised packet header for image transmission, their approach does not address the problem of spatially clustered losses, which can severely degrade image quality. The proposed algorithm's deliberate avoidance of loss clustering and use of hierarchical reconstruction metrics (including the centroid distance,  $DIST$ ) provide robustness in scenarios with high and unpredictable packet loss, as demonstrated both in simulation and in a real urban mesh network.

A summary comparison of key features is presented in Tab. 3:

The results obtained in this study demonstrate that the proposed approach can maintain high reconstruction quality ( $SSIM > 0.6$ ,  $DIST < 0.1$  px) even at fragment delivery rates as low as 40 %, outperforming retransmission-based methods in terms of resilience and energy efficiency in mesh network scenarios.

This article presents an innovative thermogram fragmentation algorithm optimized for transmission in LoRa-based mesh networks characterized by limited bandwidth and high packet loss. The developed solution employs a three-layer fragmentation strategy enabling the division of  $32 \times 24$  pixel thermograms into 16, 24, or 32 fragments with adaptive redundancy and a loss compensation mechanism. The algorithm implements pixel permutation to prevent loss clustering and hierarchical reconstruction utilizing redundant information in the form of average values for regions of varying sizes.

Simulation studies conducted on a set of 24 thermograms demonstrated gradual, linear degradation in reconstruction quality with increasing fragment loss. Under near-total loss conditions, the algorithm achieved a temperature error  $RMSE$  of approximately  $2.3$  °C (relative error 2.5 %), a  $PSNR$  decrease from 53 dB to 30 dB, and maintained an  $SSIM$  value of 0.3. The key metric  $DIST$ , representing the positional error of the thermogram centroid, increased only to 0.25 pixels, which constitutes less than 1 % of the image size.

Verification in a real Meshtastic network in Warsaw comprising approximately 200 devices confirmed the practical utility of the algorithm. A total of 225 thermograms were transmitted, and the receiver with the lowest availability (40 % of fragments received) still enabled thermogram reconstruction with an average  $SSIM$  value greater than 0.6 and a positional error  $DIST$  less than 0.1 pixels. A significant finding was the lack

of dependence of the fragment delivery ratio on fragment size, suggesting the dominance of other network factors over packet size in determining transmission losses. The algorithm maintains predictable and useful performance under conditions of variable network reliability, making it suitable for monitoring and detection applications in IoT infrastructure.

## Acknowledgments

This work was co-financed by Military University of Technology under research project UGB 531-000078-W600-22. The authors would like to thank the Meshtastic network community in Warsaw for their assistance in conducting the experiment, particularly Krzysztof Sprawnik, operators of the nodes: BFNP and mundek, and the students of Institute of Optoelectronics at Military University of Technology (WAT).

## Bibliography

1. Jose J., *Inferno Strife– early forest fire detection*, PhD thesis, Amal Jyothi College Of Engineering, 2019.
2. Sadi M., Zhang Y., Xie W.-F., Hossain F.A., *Forest fire detection and localization using thermal and visual cameras*, 2021 International Conference on Unmanned Aircraft Systems (ICUAS), 2021, 744–749, DOI: 10.1109/ICUAS51884.2021.9476865.
3. Trzaskawka P., Kastek M., Życzkowski M., Dulski R., Szustakowski M., Ciurapiński W., Barela J., *System for critical infrastructure security based on multispectral observation-detection module*, Electro-Optical and Infrared Systems: Technology and Applications X, SPIE, 2013, 235–246, DOI: 10.1117/12.2028740.
4. Francisco G., Roberts S., Hanna K., Heubusch J., *Critical infrastructure security confidence through automated thermal imaging*, Infrared Technology and Applications XXXII, SPIE, 2006, 1006–1017, DOI: 10.1117/12.664988.
5. Lin Y.-T., Finlayson G.D., *On the optimization of regression-based spectral reconstruction*, “Sensors”, Vol. 16, No. 16, 2021, DOI: 10.3390/s21165586.
6. Wang Z., Bovik A.C., Sheikh H.R., Simoncelli E.P., *Image quality assessment: from error visibility to structural similarity*, “IEEE Transactions on Image Processing”, Vol. 13, No. 4, 2004, 600–612, DOI: 10.1109/TIP.2003.819861.
7. Kudelka Jr M., *Image quality assessment*, [In:] WDS ‘12 Proceedings of Contributed Papers, Part I, 2012, 94–99.
8. Chiani M., Elzanaty A., *On the LoRa modulation for IoT: Waveform properties and spectral analysis*, “IEEE Internet of Things Journal”, Vol. 6, No. 5, 2019, 8463–8470, DOI: 10.1109/JIOT.2019.2919151.
9. Maleki A., Nguyen H.H., Bedeer E., Barton R., *A tutorial on chirp spread spectrum for LoRaWAN: Basics and key*

- advances*, “IEEE Open Journal of the Communications Society”, Vol. 5, 2024, 4578–4612,  
DOI: 10.1109/OJCOMS.2024.3433502.
10. Mnguni S., Mudali P., Abu-Mahfouz A.M., Adigun M., *Impact of the packet delivery ratio (PDR) and network throughput in gateway placement LoRaWAN networks*, Southern Africa Telecommunication Networks and Applications Conference (SATNAC) 2021, 301–306.
  11. Kosek-Szott K., *A survey of MAC layer solutions to the hidden node problem in ad-hoc networks*, “Ad Hoc Networks”, Vol. 10, No. 3, 2012, 635–660,  
DOI: 10.1016/j.adhoc.2011.10.003.
  12. Sjoberg K., Uhlemann E., Strom E.G., *How severe is the hidden terminal problem in VANETs when using CSMA and STDMA?*, 2011 IEEE Vehicular Technology Conference (VTC Fall), 2011, DOI: 10.1109/VETECF.2011.6093256.
  13. Jayasuriya A., Perreau S., Dadej A., Gordon S., et al., *Hidden vs. exposed terminal problem in ad hoc networks*, 2004.
  14. Allred L.G., Kelly G.E., *Lossless image compression technique for infrared thermal images*, Hybrid Image and Signal Processing III, SPIE, 1992, 230–237,  
DOI: 10.1117/12.60564.
  15. Schaefer G., Starosolski R., Zhu S.Y., *An evaluation of lossless compression algorithms for medical infrared images*, 2005 IEEE Engineering in Medicine and Biology 27th Annual Conference, 1673–1676,  
DOI: 10.1109/IEMBS.2005.1616764.
  16. Seller O., Sornin N., *Low power long range transmitter, LoRa patent describing encoding scheme*, 2014.
  17. Horé A., Ziou D., *Image quality metrics: PSNR vs. SSIM*, 20<sup>th</sup> International Conference on Pattern Recognition, 2010, 2366–2369, DOI: 10.1109/ICPR.2010.579.
  18. Kanagasingham S., Mills A.R., Kadirkamanathan V., *Distributed Kalman Filtering for Temporal Resolution Enhancement of Thermal Images*, 2023 International Symposium on Image and Signal Processing and Analysis (ISPA), DOI: 10.1109/ISPA58351.2023.10279782.
  19. Wang Z., Bovik A.C., Sheikh H.R., *Structural similarity based image quality assessment*, [In:] Digital Video image quality and perceptual coding, 2017, 225–242, CRC Press.
  20. Kim J., Kwak M., et al., *Reliable image transmission over LoRa networks*, “Issues in Information Systems”, Vol. 25, No. 1, 2024, 199–207, DOI: 10.48009/1\_iis\_2024\_117.
  21. Kim J., Jenkins J., Seol J., Kwak M., *Extending data transmission in the multi-hop LoRa network*, “Issues in Information Systems”, Vol. 23, No. 1, 2022, 292–304,  
DOI: 10.48009/3\_iis\_2022\_124.
  26. European Telecommunications Standards Institute (ETSI) (2011): Electromagnetic compatibility and Radio spectrum Matters (ERM); System Reference document (SRdoc): Spectrum Requirements for Short Range Device, Metropolitan Mesh Machine Networks (M3N) and Smart Metering (SM) applications, Technical Report ETSI TR 103 055 V1.1.1, European Telecommunications Standards Institute (ETSI).
  27. Meshtastic, *Overview*, <https://meshtastic.org/docs/overview>, 2025.
  28. MeshCore – *A Deep Dive into The Latest Off-Grid Communications Software*, <https://meshunderground.com/posts/1741274143149-meshcore---a-deep-dive-into-the-latest-off-grid-communications-software>, 2025.
  29. Melexis, *MLX90640 32x24 IR array Datasheet*, Datasheet 3901090640, Melexis NV, revision 12, 2019.
  30. Melexis, *MLX90640 library functions*, <https://github.com/melexis/mlx90640-library>.
  31. scikit-image development team, *Structural similarity index*, [https://scikit-image.org/docs/stable/auto\\_examples/transform/plot\\_ssim.html](https://scikit-image.org/docs/stable/auto_examples/transform/plot_ssim.html).

## Other sources

22. Semtech Corporation, SX1272/3/6/7/8: LoRa Modem Designer’s Guide AN1200.13, 2013.
23. European Telecommunications Standards Institute, ETSI EN 300 220-2 V3.1.1: Electromagnetic compatibility and Radio spectrum Matters (ERM); Short Range Devices (SRD); Radio equipment to be used in the 25 MHz to 1000 MHz frequency range with power levels ranging up to 500 mW; Part 2: Harmonised Standard for access to radio spectrum, 2017.
24. Semtech Corporation, *Predicting LoRaWAN Capacity*, Technical report, 2024.
25. CEPT/ERC, ERC Recommendation 70-03: Relating to the use of Short Range Devices (SRD), 1997, Last revised: February 2022.

# Odporna na straty metoda fragmentacji termogramów przeznaczona dla kratowych sieci IoT LoRa

**Streszczenie:** Monitorowanie środowiska za pomocą kamer termowizyjnych napotyka istotne wyzwania w obszarach zdalnych, pozbawionych infrastruktury telekomunikacyjnej komórkowej lub stacjonarnej. W artykule przedstawiono nowatorski algorytm fragmentacji do transmisji termogramów o niskiej rozdzielcości ( $32 \times 24$  piksele) w sieciach mesh LoRa, charakteryzujących się ograniczoną przepustowością i wysokim wskaźnikiem strat pakietów. Proponowana trójwarstwowa strategia fragmentacji dzieli termogramy na 16, 24 lub 32 fragmenty z adaptacyjną redundancją i mechanizmami kompensacji strat. Algorytm implementuje permutację pikseli zapobiegającą skupiskom strat oraz hierarchiczną rekonstrukcję wykorzystującą informacje nadmiarowe w postaci wartości średnich dla obszarów o różnych rozmiarach. Badania symulacyjne na 24 termogramach wykazały stopniową, liniową degradację jakości wraz ze wzrostem strat fragmentów. Przy niemal całkowitych stratach algorytm osiągnął błąd temperaturowy RMSE około  $2,3^{\circ}\text{C}$  (błąd względny 2,5 %), spadek PSNR z 53 dB do 30 dB oraz utrzymanie wartości SSIM na poziomie 0,3. Kluczowa metryka DIST, określająca błąd pozycyjny środka ciężkości termogramu, wzrosła jedynie do 0,25 piksela (mniej niż 1 % wielkości obrazu). Weryfikacja w rzeczywistej sieci Meshtastic w Warszawie, obejmującej około 200 urządzeń, potwierdziła praktyczną użyteczność algorytmu. Po przesłaniu 225 termogramów odbiorniki z 40 % dostarczalnością fragmentów nadal umożliwiały rekonstrukcję ze średnią wartością SSIM  $>0,6$  i błędem DIST  $<0,1$  piksela, co świadczy o skuteczności algorytmu w zastosowaniach monitoringu IoT.

**Słowa kluczowe:** termowizja, fragmentacja obrazu, sieć kratowa LoRa, rekonstrukcja termogramów, Internet Rzeczy

## Krzysztof Sawicki, Phd Eng.

krzysztof.sawicki@wat.edu.pl  
ORCID: 0000-0002-1368-3854

He graduated from the Faculty of Electronics at the Military University of Technology (WAT) in 2009 and obtained his PhD from the same university in 2019 with a dissertation on steganography in wireless networks. His research interests include wireless networks, ICT security, steganography, and embedded systems, with a focus on their application in infrared and thermal imaging technologies..



## Tomasz Sosnowski, Phd Eng.

tomasz.sosnowski@wat.edu.pl  
ORCID: 0000-0003-4082-8366

He is a 1993 graduate of the Faculty of Electronics at the Military University of Technology. He received his PhD in technical sciences in 2003. His work focuses on issues related to the design and programming of digital systems, digital signal analysis, thermographic image analysis, and the application of microprocessor and programmable circuits in infrared technology.



## Mariusz Mścichowski, MSc Eng.

mariusz.mscichowski@wat.edu.pl  
ORCID: 0000-0002-0079-1960

He is a graduate of the Faculty of Electronics at the Military University of Technology. His professional interests are focused on digital electronic measurement systems and Fused Deposition Modeling (FDM) for rapid prototyping.

